WiProfile: unlocking diffraction effects for sub-centimeter target profiling using commodity WiFi devices

Zhiyun Yao, Xuanzhi Wang, Kai Niu, Rong Zheng, Junzhe Wang, Daqing Zhang

WiProfile: Unlocking Diffraction Effects for Sub-Centimeter Target Profiling Using Commodity WiFi Devices

Zhiyun Yao[†], Xuanzhi Wang[†], Kai Niu[♮], Rong Zheng[‡], Junzhe Wang[†], Daqing Zhang[†♯]
[†]School of Computer Science, Peking University, [♮]Beijing Xiaomi Mobile Software Company Ltd.,
[‡]Dept. of Computing and Software, McMaster University, [♯]SAMOVAR, Telecom SudParis, IP Paris
zhiyunyao@stu.pku.edu.cn, xuanzhiwang@stu.pku.edu.cn, xjtunk@pku.edu.cn,
rzheng@mcmaster.ca, wjz020606@stu.pku.edu.cn, dqzhang@sei.pku.edu.cn

ABSTRACT

Despite intensive research efforts in radio frequency non-contact sensing, capturing fine-grained geometric properties of objects, such as shape and size, remains an open problem using commodity WiFi devices. Prior attempts are incapable of characterizing object shape or size because they predominantly rely on weak signals reflected off objects in a very small number of directions. In this paper, motivated by the observation that the diffracted signals around an object between two WiFi devices carry the contour information of the object, we formulate the problem of reconstructing the 2D target profile and develop WiProfile, the first WiFi-based system that unlocks the diffraction effects for target profiling. We introduce a CSI-Profile model to characterize the relationship between the CSI measured at different target positions and the target profile in the diffraction zone. With suitable approximations, the inverse problem of deriving the target profile from CSI can be solved by the inverse Fresnel transform. To mitigate CSI measurement errors on commodity WiFi devices, we propose a novel antenna placement strategy. Comprehensive experiments demonstrate that WiProfile can accurately reconstruct profiles with median absolute errors of less than 1 cm under various conditions, and effectively estimate the profiles of everyday objects of diverse shapes, sizes, and materials. We believe this work opens up new directions for fine-grained target imaging using commodity WiFi devices.

CCS CONCEPTS

• **Human-centered computing → Ubiquitous and mobile computing systems and tools**; *Ubiquitous computing*; *Mobile computing*; Ambient intelligence.

KEYWORDS

WiFi Imaging, WiFi Sensing, Diffraction, CSI-Profile Model

ACM Reference Format:
Zhiyun Yao, Xuanzhi Wang, Kai Niu, Rong Zheng, Junzhe Wang, and Daqing Zhang. 2024. WiProfile: Unlocking Diffraction Effects for Sub-Centimeter Target Profiling Using Commodity WiFi Devices. In *International Conference On Mobile Computing And Networking (ACM MobiCom '24), September 30–October 4, 2024, Washington D.C., DC, USA.* ACM, New York, NY, USA, 15 pages.

1 INTRODUCTION

WiFi-based non-contact sensing, repurposing ubiquitous WiFi devices to sense and analyze human behaviors without any physical attachment, has received considerable attention in both the research and industrial communities. A multitude of applications boasting impressive performance have been implemented, including intrusion detection [18, 19, 46, 52], indoor tracking [20, 21, 33, 45], activity recognition [17, 26, 30, 37], gesture recognition [8, 9, 25, 42], and vital sign monitoring [22, 23, 36, 48]. However, due to the constrained bandwidth (e.g., 20 MHz) and the limited number of antennas (e.g., three), target imaging with the goal of capturing fine-grained geometric properties of objects, such as shape and size, remains an open problem using commodity WiFi devices.

Target imaging is critical to object recognition and quality control, and can find applications in various fields, such as industrial automation, robotics, healthcare, and security. Unlike camera-based approaches, WiFi-based target imaging is less susceptible to environmental factors such as lighting conditions, smoke, and dust. Furthermore, since WiFi signals can permeate opaque materials like foam or paper, they allow the inspection of internal objects without the need to unwrap or remove packaging.

As listed in Table 1, prior attempts predominantly utilize signals reflected off objects [12, 14, 16, 31, 34]. Their coarse

Table 1: Existing works on WiFi-based target imaging.

Reference	Principle	Size Estimation	Device
WiPose [14]	Reflection	✘	Commodity
WiSIA [16]	Reflection	✘	Commodity
GoPose [34]	Reflection	✘	Commodity
Wision [12]	Reflection	>5 cm	USRP
Wiffract [31]	Scattering	✘	Commodity
WiProfile	**Diffraction**	**1 cm**	**Commodity**

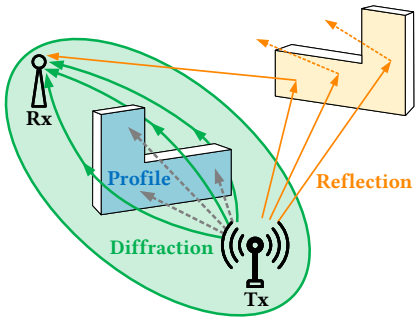

Figure 1: Specular reflection and diffraction effects.

imaging performance can be informative in terms of detecting and localizing objects, but is incapable of characterizing object shape or size [31]. The fundamental reason is that the surfaces of everyday objects appear smooth to the relatively long wavelength of WiFi signals, and only reflect off the signals in a very small number of directions – a phenomenon called specular reflection [31]. For example, the "Reflection" in Figure 1 illustrates a common setup in previous studies, where a yellow L-shaped object is placed away from the Line of Sight (LoS) path between a pair of WiFi transmitter (Tx) and receiver (Rx). Only a portion of reflected signals can be intercepted by Rx owing to specular reflection. Additionally, the signals are more attenuated as they need to traverse longer paths compared to the LoS path.

On the other hand, when a target with a clear edge obstructs the LoS path between Tx and Rx (e.g., the blue object in Figure 1), diffraction is pronounced since the transmitted signals can "bend" around the edges of the target. Importantly, the received diffracted signals carry the contour information of the target in accordance to the Huygens–Fresnel principle [2]. Exploiting diffraction for target imaging, however, is non-trivial in practical WiFi systems.

- First, since most of the surface area of the target facing the Tx or Rx remains blocked or shadowed, one can at best estimate the contour of its largest cross-section, oriented perpendicular to the LoS path, from the diffracted signals. We refer to this cross-section as the *target profile*. Therefore, instead of 3D shapes, we aim to reconstruct the 2D profile of objects without internal holes, termed as *target profiling*.
- Second, for a stationary target, the received signal is a mixture of diffracted signals around it. Therefore, the target profile information is "buried" in the received signal. To reconstruct the profile, inspired by Inverse Synthetic Aperture Radar (ISAR) imaging [3, 4, 29], we let the target move in the plane perpendicular to the LoS path. A CSI-Profile model is derived to characterize the relationship between the CSI measured at different target positions and the target profile.
- Third, determining the target profile from the CSI measurements necessitates solving the inverse problem to the CSI-Profile model, which is extremely sensitive to noise. Fortunately, with suitable approximations, a robust solution can be obtained by the inverse Fresnel transform [13].
- Fourth, a setup with physically separated Tx and Rx devices will introduce CSI measurement errors due to unsynchronized clocks [44]. Conventional techniques [49, 50] that employ two closely situated Rx antennas to cancel phase errors are no longer effective since the received signals from both antennas contain strong dynamic components due to diffraction and target movements. To overcome this challenge, we introduce an auxiliary Rx antenna placed next to the Tx as reference to calibrate the received signals on the primary Rx antenna.

Building upon the theoretical foundation and the novel CSI error mitigation technique, we develop WiProfile, a WiFi-based target profiling system using only a pair of commodity WiFi devices. To achieve optimal performance, WiProfile employs a controlled setup, where the target to be profiled moves at a constant velocity along a linear trajectory between the transceivers, perpendicular to the LoS path. WiProfile has been evaluated using a variety of target shapes in diverse surrounding environments. Comprehensive experiments show that WiProfile can achieve sub-centimeter median absolute errors under various conditions. Furthermore, it can effectively estimate the profiles of everyday objects of diverse shapes, sizes, and materials. To the best of our knowledge, this is the first work that unlocks the diffraction effects of WiFi signals for fine-grained target profiling.

The main contributions of this paper are summarized as follows:

- We introduce a CSI-Profile model to characterize the relationship between the CSI measured at different target positions in the diffraction zone and the target profile.
- We propose an analytical solution to determine the target profile from CSI and a novel antenna placement strategy to mitigate CSI measurement errors on commodity WiFi devices.
- We develop WiProfile, a WiFi-based target profiling system using only a pair of commodity WiFi devices.
- Comprehensive experiments demonstrate the effectiveness of WiProfile under various conditions, yielding sub-centimeter median absolute errors.

2 TARGET PROFILING BASED ON DIFFRACTION EFFECTS

In this section, we begin with an analytical CSI-Profile model to characterize the relationship between the target profile and the CSI induced by the target when it obstructs the LoS path between a pair of WiFi transceivers. The inverse problem of determining the target profile from CSI is then solved, followed by a discussion on operation conditions of target profiling.

2.1 CSI-Profile Model

Consider the scenario in Figure 1, where a target (the L-shaped object in blue) is located between a transmitter (Tx) and a receiver (Rx). As shown in Figure 2a, we define a global coordinate frame (X, Y, Z) with Tx and Rx positioned along the Y-axis at coordinates $(0, -y_T, 0)$ and $(0, y_R, 0)$, respectively. The X-Z plane encompasses the target's largest cross-section oriented perpendicular to the Y-axis. The thickness of the target is the distance between two opposite surfaces that are parallel to the X-Z plane and tangential to the target. Under the assumption that its thickness is much smaller than the Tx-Rx separation $y_T + y_R$, the target can be approximated as a 2D shape and its profile S is defined as its 2D projection on the X-Z plane. Note that under the 2D projection, different orientations of the same object may result in distinct profiles. For example, the profile of the object with its elongated bottom edge misaligned with the X-axis is narrower than that of the object whose bottom edge aligns with the X-axis. However, in both cases, the height of the profile remains the same.

As illustrated in Figure 2b, S can be characterized by two functions $u_S(x)$ and $l_S(x)$, namely,

$$S = \{(x, z) \mid x \in [W_L, W_R], z \in [l_S(x), u_S(x)]\}, \tag{1}$$

where W_L and W_R are the left and right limits of the target profile along X-axis.

When a target is located between a pair of WiFi transceivers, the diffraction effects are pronounced [11, 51, 53]. According to the Fresnel–Kirchhoff diffraction formula [2], the diffracted signal originated from Tx and received at Rx *around* region S (or equivalently *through* $\bar{S}$, the area outside S in the X-Z plane) can be expressed as the integral of $f(x, z)$ over the unbounded region $\bar{S}$:

$$H_{\bar{S}} = \iint_{\bar{S}} f(x, z)\, dxdz, \tag{2}$$

where $f(x, z)$ is a basic function to characterize the diffraction signal induced by only a single point in the space:

$$f(x, z) = \frac{A}{2j\lambda} \frac{\cos\alpha_T(x, z) + \cos\alpha_R(x, z)}{r_T(x, z)\, r_R(x, z)} e^{-jk[r_T(x,z) + r_R(x,z)]}, \tag{3}$$

Table 2: Key notations.

Symbol	Definition
y_T	the distance between Tx and the origin
y_R	the distance between Rx and the origin
$r_T(x, z)$	the distance between Tx and a point $(x, 0, z)$
$r_R(x, z)$	the distance between Rx and a point $(x, 0, z)$
$\alpha_T(x, z)$	the space angle between Y-axis and Tx-$(x, 0, z)$
$\alpha_R(x, z)$	the space angle between Y-axis and Rx-$(x, 0, z)$

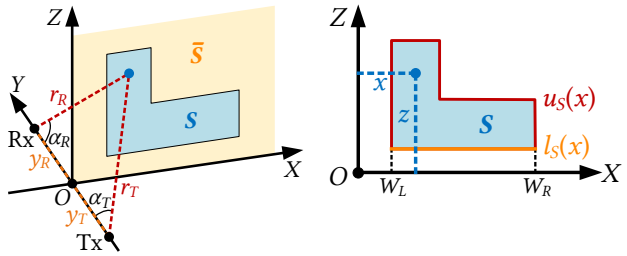

(a) Global coordinate frame. **(b) Region S.**

Figure 2: Diffraction scenario.

where A is the amplitude of the transmitted signal, j is the imaginary unit, λ is the signal wavelength, and k is the signal wavenumber given by $k = \frac{2\pi}{\lambda}$. y_T, y_R, r_T, r_R, α_T, and α_R are defined in Table 2 and illustrated in Figure 2a.

Since $\bar{S}$ is unbounded, Equation (2) cannot be calculated directly. Fortunately, according to Babinet's Principle [35], we have $H_{\bar{S}} = H_{wo} - H_S$, where $H_{wo} = \iint f(x, z)\, dxdz$ and $H_S = \iint_S f(x, z)\, dxdz$. H_{wo}, calculated as the infinite integral of $f(x, z)$ over the X-Z plane, is the received signal in absence of the target. Given a fixed deployment of Tx-Rx pair, it is a constant independent of the target position. H_S, the integral of $f(x, z)$ over the region S, on the other hand, corresponds to the signal diffracted through S when $\bar{S}$ is obstructed instead. It changes when the target position changes.

Measuring $H_{\bar{S}}$ for a fixed target is insufficient to determine its profile. Next, we consider the received signals as the target undergoes linear movements along the X-axis, as shown in Figure 3. Let $S(d_t)$ denote the 2D profile of the target when it shifts by a displacement d_t. From Equation (1), we have

$$S(d_t) = \{(x,z) \mid x \in [W_L + d_t, W_R + d_t], z \in [l_S(x - d_t), u_S(x - d_t)]\}.$$

Without loss of generality, we let $W_L = -\frac{W}{2}$ and $W_R = \frac{W}{2}$, where W is the width of the profile. Define

$$u(x) = \begin{cases} u_S(x), & x \in [W_L, W_R], \\ 0, & \text{otherwise.} \end{cases}$$

and

$$l(x) = \begin{cases} l_S(x), & x \in [W_L, W_R], \\ 0, & \text{otherwise.} \end{cases}$$

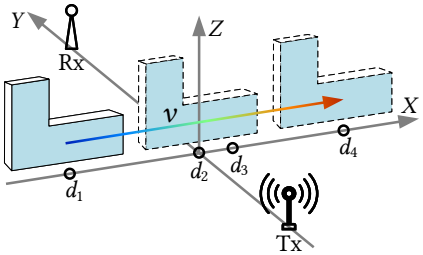

Figure 3: The target moves along the X-axis.

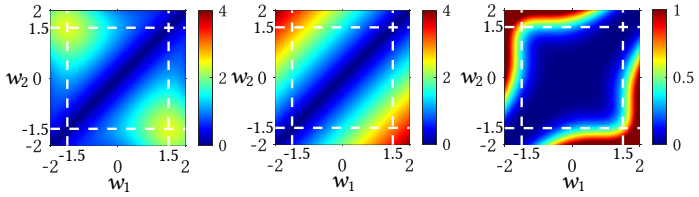

(a) $|F(w_1, w_2)|$. **(b) $|w_2 - w_1|$.** **(c) Difference.**

Figure 4: Approximation of the profile function.

Then, upon substituting the region S with $S(d_t)$ in $H_S = \iint_S f(x,z)\,dxdz$, the dynamic component $H_S(d_t)$ is given by

$$\begin{aligned} H_S(d_t) &= \iint_{S(d_t)} f(x,z)\,dxdz = \iint_S f(x+d_t,z)\,dxdz \\ &= \int_{-\infty}^{+\infty}\left[\int_{l(x)}^{u(x)} f(x+d_t,z)\,dz\right]dx. \end{aligned} \tag{4}$$

The second equality is the result of replacing the integration variable x by $x+d_t$. The diffracted signal $H_{\bar{S}}(d_t)$ is a superposition of a static component H_{wo} and a dynamic component $H_S(d_t)$ as the target moves. That is,

$$H_{\bar{S}}(d_t) = H_{wo} - H_S(d_t). \tag{5}$$

Under the condition that $\max_x\{u(x) - l(x)\} \ll y_T + y_R$, namely, the height of the target profile is much smaller than the Tx-Rx separation, we can show that

$$f(x+d_t,z) \approx f(x+d_t,0)e^{-jk\rho_0 z^2}, \tag{6}$$

where $\rho_0 = \frac{1}{2y_T} + \frac{1}{2y_R}$. The detailed derivation can be found in Appendix A.1. Substituting Equation (6) into Equation (4), we have

$$H_S(d_t) \approx \int_{-\infty}^{+\infty}\left[\int_{l(x)}^{u(x)} f(x+d_t,0)e^{-jk\rho_0 z^2}\,dz\right]dx. \tag{7}$$

Noting that $f(x+d_t,0)$ is independent of z, we can factor it out of the inner integral so that

$$H_S(d_t) \approx \int_{-\infty}^{+\infty} \underbrace{\int_{l(x)}^{u(x)} e^{-jk\rho_0 z^2}\,dz}_{①}\ \underbrace{f(x+d_t,0)}_{②}\,dx. \tag{8}$$

Equation (8) is an integral of the product of two terms, ① and ②. Next, we explain their physical meanings and implications on the dynamic component $H_S(d_t)$.

The Profile Function. Term ① is determined by the integral limits $u(x)$ and $l(x)$, i.e., the upper and lower bound functions of the profile with the relation $u(x) \geq l(x)$. Therefore, we refer to ① as the "profile function", and denote it by $P(x)$. That is,

$$P(x) = \int_{l(x)}^{u(x)} e^{-jk\rho_0 z^2}\,dz. \tag{9}$$

Interestingly, we observe that the magnitude of the profile function (i.e., $|P(x)|$) appears to distinctly delineate the target profile. Since the integral lacks an antiderivative that can be expressed using elementary functions, we explain this phenomenon through numerical simulations. Letting $a = \sqrt{k\rho_0}$ and $z = \frac{1}{a}\tilde{z}$, Equation (9) is rewritten to move k and ρ_0 into the integral variable $\tilde{z}$, as follows:

$$P(x) = \frac{1}{a}\int_{w_1}^{w_2} e^{-j\tilde{z}^2}\,d\tilde{z} = \frac{1}{a}F(w_1,w_2), \tag{10}$$

where $w_1 = a{\cdot}l(x)$, $w_2 = a{\cdot}u(x)$, and $F(w_1,w_2) = \int_{w_1}^{w_2} e^{-j\tilde{z}^2}\,d\tilde{z}$. We will investigate the impacts of k and ρ_0 in Section 2.3.

Figure 4 shows the heatmaps of $|F(w_1,w_2)|$, $|w_2 - w_1|$, and their absolute difference with respect to w_1 and w_2. As illustrated in Figure 4c, when both w_1 and w_2 fall within the interval $[-1.5, 1.5]$, the pair (w_1, w_2) lies within the white box in the heatmaps, resulting in a negligible absolute difference, i.e., $|F(w_1,w_2)| \approx |w_2 - w_1|$. Hence,

$$|P(x)| = \frac{1}{a}|F(w_1,w_2)| \approx \frac{1}{a}|w_2 - w_1| = u(x) - l(x). \tag{11}$$

Therefore, the magnitude of the profile function $|P(x)|$ represents the difference between the upper and lower bound functions. When the lower bound function $l(x)$ is constant, this difference gives the upper bound function $u(x)$, effectively delineating the target profile.

The Displacement Function. Term ② is a function of d_t, i.e., the target's displacement. Therefore, we refer to ② as the "displacement function", and denote it by $D(x+d_t)$. That is,

$$D(x+d_t) = f(x+d_t,0). \tag{12}$$

As an illustration, consider the scenario depicted in Figure 3, where an L-shaped object moves from $d_1 = -0.3$ m to $d_4 = 0.3$ m along the X-axis. Figure 5a illustrates the amplitude of the displacement function. It is symmetric and peaks when the target is right in between Tx and Rx (i.e., $d_2 = 0$ m). Figure 5b illustrates the displacement function in the IQ plane. As the target moves from $d_2 = 0$ m to $d_4 = 0.3$ m, the diffraction path lengthens, causing both the amplitude and phase of the displacement function to decrease. This results in a clockwise spiral rotation. Therefore, the displace-

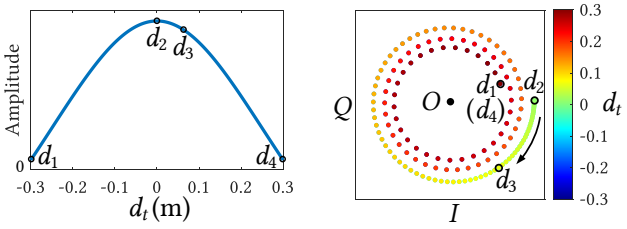

(a) Amplitude. (b) In the IQ plane.

Figure 5: The displacement function $D(d_t)$.

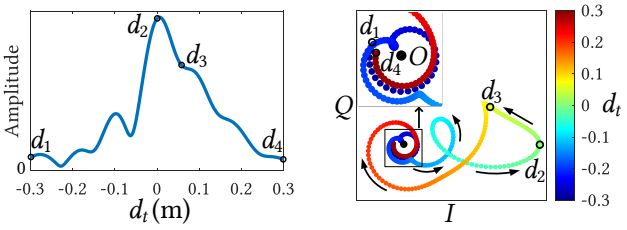

(a) Amplitude. (b) In the IQ plane.

Figure 6: The dynamic component $H_S(d_t)$.

ment function captures the relative positional information between the target and the transceivers.

Substituting $P(x)$ and $D(x + d_t)$ in place of Term ① and ②, Equation (8) becomes

$$H_S(d_t) = \int_{-\infty}^{+\infty} P(x)\, D(x + d_t)\, dx. \tag{13}$$

It immediately becomes apparent that Equation (13) represents the convolution between $P(-x)$ and $D(x)$ evaluated at displacement d_t, or, $H_S(d_t) = P(-x) * D(x)$, where $*$ is the convolution operator.

Figure 6 shows the amplitude and the IQ plot of the dynamic component $H_S(d_t)$ calculated using Equation (13). From Figure 6a, it can be seen that unlike the displacement function, the amplitude of the dynamic component is not symmetric. This is due to the asymmetric profile of the L-shape. Additionally, when the target is relatively far away from the LoS path between Tx and Rx (i.e., $|d_t| > 0.2$ m), the amplitude of the dynamic component is small; as the target approaches the LoS path (i.e., $d_t \to 0$ m), the amplitude increases due to heightened obstruction. Figure 6b shows that slight movements of the target result in discernible phase differences in the IQ plot. Additionally, when the target is relatively far away from the LoS path (i.e., $|d_t| > 0.2$ m), the dynamic component circles around the origin with a zero mean. This allows us to estimate the static component as the average of these CSI samples.

2.2 Solving for the Target Profile

To this end, we have established the CSI-Profile model to characterize the relationship between the ideal CSI, the target profile and the target positions relative to the Tx and Rx. In this section, we solve the inverse problem, namely, the task of determining the target profile from the ideal CSI at known target positions. It is worth noting that the assumption of known target positions holds validity in real-world scenarios. For instance, in a factory assembly line, objects are conveyed using a belt with a known speed and direction.

Equation (5) shows that the ideal CSI consists of two components: a static component H_{wo} that is independent of the target positions and a dynamic component $H_S(d_t)$ that changes as the target moves along the X-axis. Therefore, we first estimate and eliminate the static component from the ideal CSI signal to obtain the dynamic component, i.e., $H_S(d_t) = H_{wo} - H_{\bar{S}}(d_t)$.

Next, we determine the target profile from the dynamic component. Since the displacement function $D(x)$ is known, one direct way to solve for $P(x)$ is through deconvolution, namely, by taking the ratio of $H_S(d_t)$ and $D(x)$ in the frequency domain and then performing inverse Fourier transform. However, the solution is extremely sensitive to noise in regions where the spectral magnitude of $D(x)$ is close to zero [27]. Inspired by the work in MRI [13], we resort to an alternative representation using the *Fresnel transform*:

$$H_S(d_t) \approx \int_{-\infty}^{+\infty} P(x)\, D(d_t) e^{-jk\rho_0\left(x^2+2d_t x\right)}\, dx. \tag{14}$$

The approximation is due to the following equation:

$$D(x + d_t) \approx D(d_t) e^{-jk\rho_0\left(x^2+2d_t x\right)}. \tag{15}$$

See Appendix A.2 for the detailed derivation.

Though Equation (14) looks complicated, it is actually an easily analyzable integral transformation. Specifically, the profile function $P(x)$ can be obtained by an inverse Fresnel transform:

$$P(x) = \int_{-\infty}^{+\infty} \frac{k\rho_0}{\pi} \frac{H_S(d_t)}{D(d_t)} e^{jk\rho_0\left(x^2+2xd_t\right)}\, dd_t. \tag{16}$$

The right hand of Equation (16) contains an infinite integral. In practice, the length of the displacement is often limited. Under this constraint, Equation (16) is subsequently rewritten as

$$\hat{P}(x) = \int_{-\frac{L}{2}}^{\frac{L}{2}} \frac{k\rho_0}{\pi} \frac{H_S(d_t)}{D(d_t)} e^{jk\rho_0\left(x^2+2xd_t\right)}\, dd_t, \tag{17}$$

where L denotes the displacement distance.

Finally, the magnitude of the estimated profile function gives the difference between the upper and lower bound functions:

$$\hat{u}(x) - \hat{l}(x) = \left|\hat{P}(x)\right|. \tag{18}$$

For objects with a wide, flat bottom (e.g., a cuboid, cylinder, and cone), the lower bound function is constant. This dif-

ference is thus proportional to the upper bound function, namely, the target profile.

2.3 Operation Conditions

Several approximations have been made in the CSI-Profile model and the subsequent solution to the inverse problem. Next, we delve into the conditions such that the estimation in Section 2.2 remains accurate.

2.3.1 Target Height. Equation (11) is valid under the condition that both w_1 and w_2 fall within the interval $[\underline{-1.5}, 1.5]$, meaning a limit of the target height. Letting $|w| = \sqrt{k\rho_0}\cdot|z| < 1.5$, we have the empirical maximum height as follows:

$$|z| < \frac{1.5}{\sqrt{k\rho_0}} = \frac{1.5}{\sqrt{\frac{\pi}{\lambda}\left(\frac{1}{y_T}+\frac{1}{y_R}\right)}}. \tag{19}$$

Equation (19) shows that the target height is limited by the Tx-Rx separation ($y_T + y_R$) and the signal wavelength (λ). A longer Tx-Rx separation or signal wavelength contribute to a larger maximum height. For example, with WiFi transceivers operating at the center frequency of 5.32 GHz and placed 1 m apart ($y_T = y_R = 0.5$ m), Equation (19) gives $|z| < 10$ cm, and the maximum height is 20 cm. When the target height exceeds 20 cm, the profiling accuracy decreases.

2.3.2 Tx-Rx Separation. The Tx-Rx separation affects the profiling accuracy in two ways. When the Tx and Rx are far apart, the signal-to-noise ratio of the received signal is low, resulting in a lowered profiling accuracy. Conversely, a shorter Tx-Rx separation imposes limitations on the maximum height and thickness of the target. Consequently, the profiling accuracy drops when the target height exceeds the maximum height. Hence, to achieve accurate estimations, it is important to select an appropriate Tx-Rx separation based on the rough dimension of the target.

2.3.3 Displacement Distance. Due to the truncation of the diffracted signal in Equation (17), the displacement distance L significantly impacts the profiling accuracy. Its effect is akin to spatial windowing in radars of finite aperture. As indicated by signal processing principles [28], a larger window size implies more captured signal, and thus increased accuracy of the transformation. However, in practice, this is not always true for a larger L. Specifically, as the target moves farther from the LoS path, the amount of diffraction rapidly diminishes, while reflection intensifies. At a considerable distance, the reflection signal becomes dominant, devoid of any profile information, and the accuracy drops consequently. Therefore, the displacement distance L should be selected with careful consideration of both the Tx-Rx separation and the signal wavelength.

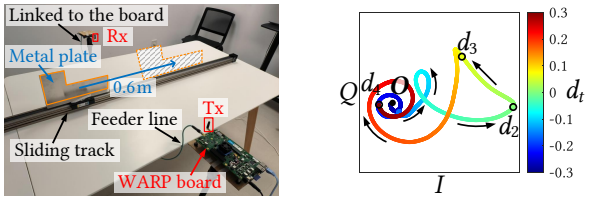

(a) WARP setup. **(b) Raw CSI in the IQ plane.**

Figure 7: Experiments on the WARP board.

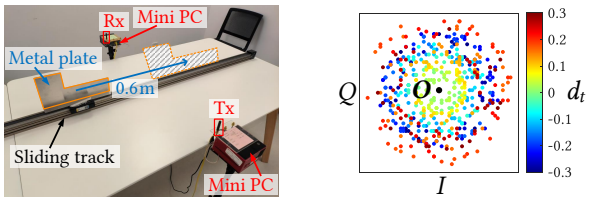

(a) Commodity devices setup. **(b) Raw CSI in the IQ plane.**

Figure 8: Experiments on the commodity WiFi devices.

3 TARGET PROFILING USING COMMODITY WIFI DEVICES

In this section, we first validate the CSI-Profile model through measurements on a software defined radio platform and show the non-trivial nature of obtaining accurate estimations using commodity WiFi devices. Then, we propose a novel antenna placement strategy to overcome the challenge of such devices. Finally, we present WiProfile, a WiFi-based target profiling system using only a pair of commodity WiFi devices.

3.1 A Validation Study

To validate the CSI-Profile model and the performance of target profiling, we conduct experiments both on a software ratio platform (i.e., WARP v3 hardware [5]) and commodity WiFi devices (i.e., Intel 5300 WiFi cards [10]).

As shown in Figure 7a, the two radio interfaces on the same WARP board are configured as the Tx and Rx, respectively. Being on the same board ensures the two interfaces to be perfectly synchronized. The Tx sends WiFi packets at a rate of 500 pkt/s, modulated to the center frequency of 5.32 GHz with a channel bandwidth of 20 MHz. A sliding track, aligned with the perpendicular bisector of the transceiver pair, moves an L-shaped metal plate over a distance of 0.6 m at a constant speed of 0.12 m/s. Omnidirectional antennas are utilized on both the Tx and Rx, placed 1 m apart. Figure 7b illustrates the IQ plot of the measured CSI, displaying a notable agreement with the analytical model depicted in Figure 6b.

Next, as shown in Figure 8a, we replace the WARP board with a pair of commodity WiFi devices, one serving as Tx and the other as Rx. The rest of the experimental setup remains the same. The measured CSI is depicted in Figure 8b. The lack

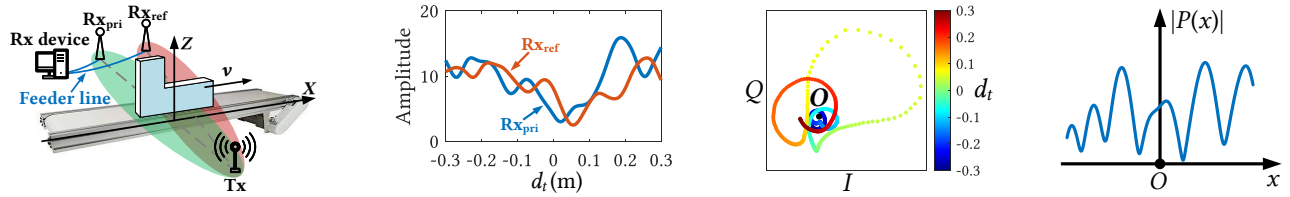

(a) Conventional antenna layout. (b) Amplitude of two antennas. (c) CSI quotient. (d) Estimated profile.

Figure 9: Experiments under conventional antenna layout.

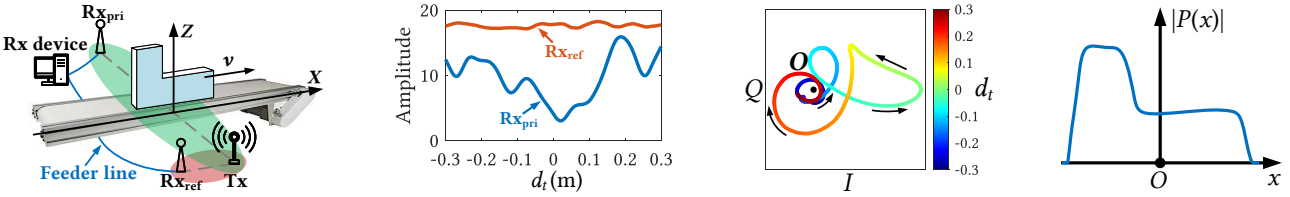

(a) WiProfile's antenna layout. (b) Amplitude of two antennas. (c) CSI quotient. (d) Estimated profile.

Figure 10: Experiments under WiProfile's antenna layout.

of any discernible pattern can be attributed to the Central Frequency Offset (CFO), Sampling Frequency Offset (SFO), and Packet Boundary Detection (PBD) errors between the two devices due to unsynchronized clocks [44].

To mitigate these errors, previous work employed the ratio of received signals from two antennas attached to the same Rx device [49, 50]. Figure 9a–9d illustrate the conventional antenna layout, the amplitude of received signals from the two antennas, the IQ plot of the CSI quotient, and the subsequent profile estimated using Equation (17), respectively. We find a significant discrepancy between the estimated and the actual profile of the L-shaped target.

The failure of the conventional techniques on commodity devices arises from the presence of strong dynamic components in the received signals from both antennas, originating from the diffraction caused by the moving target. As depicted in Figure 9a, in the conventional antenna layout, the two receiving antennas are placed adjacently, with Rx_{pri} denoting the primary receiving antenna and Rx_{ref} denoting the reference receiving antenna. The raw CSI readings from Rx_{pri} can be expressed as

$$\widetilde{H}_{\bar{S},\text{pri}}(t) = e^{-j\phi(t)} H_{\bar{S},\text{pri}}(t), \tag{20}$$

where $\phi(t)$ denotes time-varying phase errors introduced by unsynchronized clocks, and $H_{\bar{S},\text{pri}}(t)$ is the ideal CSI between the Tx and Rx_{pri}, consisting of a static and a dynamic component according to Equation (5):

$$H_{\bar{S},\text{pri}}(t) = H_{wo,\text{pri}} - H_{S,\text{pri}}(t). \tag{21}$$

Due to the short distance between Rx_{ref} and Rx_{pri}, the raw CSI readings from Rx_{ref} $\widetilde{H}_{\bar{S},\text{ref}}(t)$ can be expressed similarly, with "pri" in the subscript replaced with "ref". Thus, the CSI quotient of the two antennas is given by

$$Q(t) = \frac{\widetilde{H}_{\bar{S},\text{pri}}(t)}{\widetilde{H}_{\bar{S},\text{ref}}(t)} = \frac{\cancel{e^{-j\phi(t)}}[H_{wo,\text{pri}} - H_{S,\text{pri}}(t)]}{\cancel{e^{-j\phi(t)}}[H_{wo,\text{ref}} - H_{S,\text{ref}}(t)]}. \tag{22}$$

Clearly, the phase errors can be removed. However, since both $H_{S,\text{pri}}(t)$ and $H_{S,\text{ref}}(t)$ are non-negligible in Equation (22), we cannot easily disentangle the diffraction induced dynamic components from either CSI (Figure 9b). As illustrated in Figure 9c, although the CSI quotient $Q(t)$ shows noticeable patterns, the amplitude and phase information is corrupted, making it impossible to recover the target profile (Figure 9d).

3.2 Antenna Placement to Disentangle Dynamic Components

To address the aforementioned issue, we propose a novel antenna placement strategy. The key idea is to obtain a "reference CSI" devoid of dynamic components due to target movements. This can be accomplished by placing Rx_{ref} close to the Tx, and Tx-Rx_{ref} should be in parallel to the moving direction of the target, as illustrated in Figure 10a. Since the magnitude of the reflected signal is low and its Doppler frequency shift is small [24, 39, 40], the CSI from Rx_{ref} is dominated by the static component. Under this configuration, the CSI quotient of the two antennas becomes

$$\begin{aligned} Q_{\bar{S}}(t) &= \frac{\widetilde{H}_{\bar{S},\text{pri}}(t)}{\widetilde{H}_{\bar{S},\text{ref}}(t)} = \frac{\cancel{e^{-j\phi(t)}}[H_{wo,\text{pri}} - H_{S,\text{pri}}(t)]}{\cancel{e^{-j\phi(t)}}[H_{wo,\text{ref}} - H_{S,\text{ref}}(t)]} \\ &= \frac{H_{wo,\text{pri}} - H_{S,\text{pri}}(t)}{H_{wo,\text{ref}} + \epsilon(t)} \approx \frac{H_{wo,\text{pri}}}{H_{wo,\text{ref}}} - \frac{H_{S,\text{pri}}(t)}{H_{wo,\text{ref}}} \\ &= Q_{wo} - Q_S(t), \end{aligned} \tag{23}$$

where $\epsilon(t)$ denotes a negligible residual dynamic component in the received signal from Rx_{ref}. The variables $Q_{wo} = \frac{H_{wo,\text{pri}}}{H_{wo,\text{ref}}}$ and $Q_S(t) = \frac{H_{S,\text{pri}}(t)}{H_{wo,\text{ref}}}$ represent the new static and the new dynamic component constituting the CSI quotient, respectively. As can be seen, the CSI quotient eliminates the phase errors. However, in the new dynamic component $Q_S(t)$, the desired dynamic component $H_{S,\text{pri}}(t)$ is scaled by the denominator $H_{wo,\text{ref}}$. Fortunately, $H_{wo,\text{ref}}$ is solely dependent on the distance between Tx and Rx_{ref} as well as the surrounding environment. Unaffected by the shape, size, and position of the target, it is a constant in a fixed setup, and can be measured in advance.

We apply the above antenna placement strategy using Intel 5300 WiFi cards, where Rx_{ref} is closely located next to the Tx within a distance of 10 cm and is connected to the Rx device via a feeder line. Figure 10b shows that the dynamic component due to target movements in the received signal from Rx_{ref} is remarkably small. Figure 10c shows that the calibrated dynamic component is in fact close to the CSI obtained through the WARP board (Figure 7b). Consequently, Figure 10d shows that there is good agreement between the estimated and the actual profile, which is far better than the case without the technique.

3.3 WiProfile System

Building upon the CSI-Profile model, the analytical solution to determine the target profile from CSI, and the novel CSI error mitigation technique, we are now in the position to present WiProfile, a WiFi-based target Profiling system using only a pair of commodity WiFi devices. Figure 11 illustrates the system diagram consisting of three key modules: *Data Acquisition*, *Signal Processing*, and *Profile Estimation*. Next, we introduce the design of each module in detail.

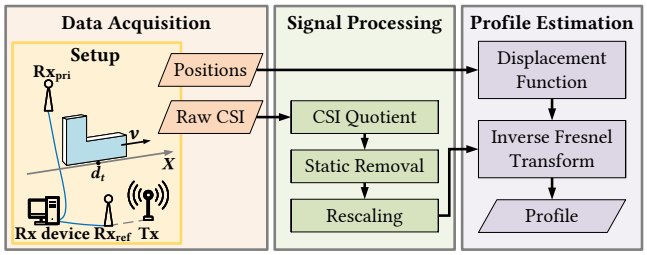

Figure 11: System diagram of WiProfile.

Data Acquisition: The target positions over time $d_t(t)$ are recorded, and raw CSI samples $\widetilde{H}_{\bar{S},\text{pri}}(t)$ and $\widetilde{H}_{\bar{S},\text{ref}}(t)$ are collected from the two antennas of the Rx device. The scaling factor $H_{wo,\text{ref}}$ of current setup is measured in advance.

Signal Processing: In this module, three steps are conducted successively. First, we mitigate CSI measurement errors by computing the CSI quotient of the primary and reference Rx antennas, i.e., $Q_{\bar{S}}(t) = \frac{\widetilde{H}_{\bar{S},\text{pri}}(t)}{\widetilde{H}_{\bar{S},\text{ref}}(t)}$. Second, to obtain the dynamic component $Q_S(t)$, we estimate the static component Q_{wo} as the average of samples measured at positions $|d_t(t)| > 0.2$ m and eliminate it from the CSI quotient. Finally, we perform rescaling to correct the contribution of $H_{wo,\text{ref}}$.

Profile Estimation: The displacement function is calculated using the positions and system parameters following Equation (12). With the displacement function and the dynamic component, we apply the inverse Fresnel transform defined in Equation (17) to obtain the profile function $\hat{P}(x)$. To suppress the sidelobe caused by the truncation, a Hann window is applied to the dynamic component [28]. Since the magnitude of the profile function $\left|\hat{P}(x)\right|$ gives the difference between the upper and lower bound functions, for objects with a wide, flat bottom (e.g., a cuboid, cylinder, and cone), it in fact captures the profile of the target. Finally, we smooth the estimated profile with a median filter.

4 PERFORMANCE EVALUATION

In this section, we conduct extensive experiments to evaluate the WiProfile system. The experimental setup is first introduced, followed by the overall performance. Next, the impacts of experimental conditions are studied, including the Tx-Rx separation, displacement distance, sample rate, and surrounding environment. Finally, we evaluate WiProfile on everyday objects of diverse shapes, sizes, and materials to demonstrate its versatility.

4.1 Experimental Setup

In this section, we introduce the implementation of WiProfile, the experimental setup, the process of acquiring ground truth, and the performance metrics.

Implementation: We use two mini PCs equipped with Intel 5300 WiFi cards as transceivers, and use the CSI-Tool [10] to acquire CSI readings. By default, the Tx is set to the injection mode to transmit WiFi packets at a rate of 500 pkt/s at the center frequency of 5.32 GHz with a channel bandwidth of 20 MHz. The Rx works in the monitor mode to capture WiFi packets from the Tx and extract CSI streams. All Tx and Rx antennas are omnidirectional. A laptop with Intel i7 CPU and 32G RAM is connected to the Rx with routers and processes the CSI readings in MATLAB to report the results. We utilize only one subcarrier to estimate the target profile.

Experimental setup: We conduct experiments in three typical indoor environments: a small meeting room (4 m × 3 m), an office (6 m × 4 m), and a lobby (10 m × 8 m). This corresponds to small, medium and large space, as shown in Figure 12. In each environment, we choose a 1.5 m × 1 m test area and deploy WiProfile following the layout shown

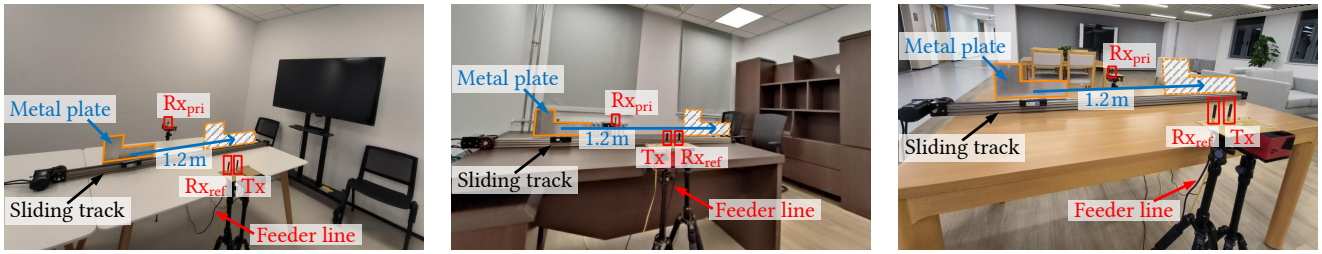

(a) Meeting room (4 m × 3 m). **(b) Office (6 m × 4 m).** **(c) Lobby (10 m × 8 m).**

Figure 12: System setup and experimental environments.

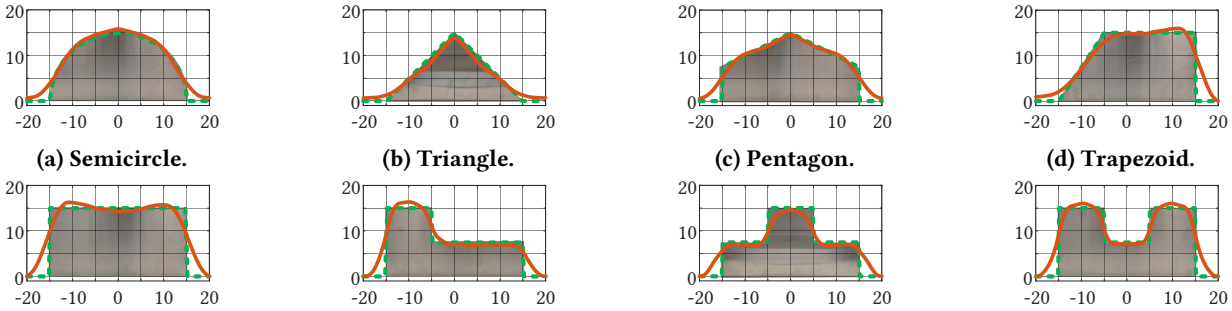

(a) Semicircle. **(b) Triangle.** **(c) Pentagon.** **(d) Trapezoid.**

(e) Rectangle. **(f) L-shape.** **(g) Inverted-T-shape.** **(h) U-shape.**

Figure 13: Estimated profiles of metal plates of eight shapes (Unit: cm).

in Figure 12. In the conducted experiments, we move the target at a constant speed of 0.12 m/s along a sliding track aligned with the perpendicular bisector of the transceiver pair. Unless otherwise specified, the default displacement distance is 1.2 m. The primary Rx antenna is positioned at a default distance of 1 m from the Tx antenna, and the reference Rx antenna is placed close to the Tx antenna within a distance of 10 cm, as discussed in Section 3.2. All antennas are elevated using tripods by 10 cm above the top of the sliding track. Following the analysis in Section 2.3, this arrangement allows a maximum target height of 20 cm.

Ground truth: We establish the ground truth of the target profile through direct measurements using a vernier caliper with a measurement accuracy of ±0.05 mm, supplemented by images captured by a camera for qualitative comparison.

Performance metrics: Let $\hat{u}(x_i)$ and $u(x_i)$ $(i \in [1, m])$ denote the estimated profile and the ground truth, respectively, where x_i is the position in X-axis for the i-th sample, and m is the total number of samples. The absolute error of the two sequences can be used to evaluate the performance at each sample, i.e., $|\hat{u}(x_i) - u(x_i)|$. Additionally, the Mean Absolute Error (MAE) and Intersection over Union (IoU) are applied as the overall evaluation metrics, which are defined as follows:

$$\text{MAE} = \frac{1}{m}\sum_{i=1}^{m}|\hat{u}(x_i) - u(x_i)|, \quad \text{IoU} = \frac{\sum_{i=1}^{m}\min\{\hat{u}(x_i), u(x_i)\}}{\sum_{i=1}^{m}\max\{\hat{u}(x_i), u(x_i)\}}.$$

4.2 Overall Performance

To evaluate the overall performance of WiProfile, we employ metal plates of eight shapes as test targets. The shapes are semicircle, triangle, pentagon, trapezoid, rectangle, L-shape, inverted-T-shape, and U-shape, as illustrated by the shaded areas in Figure 13. The thickness of the metal plates is only 0.5 mm, resulting in negligible reflected signals from the sides. For each target, we repeat the experiments five times to ensure a consistent and reliable result.

Figure 13 shows the profiles of all eight targets estimated by WiProfile (red curve). It can be observed that they closely follow the ground truth. Figure 14a shows the box plot of the absolute estimation errors. For each of the eight targets, the MAE is less than 1 cm. As the shape becomes more complicated, the performance of WiProfile slightly drops due to the windowing effect of the finite displacement distance. Figure 14b shows the IoU between the estimated profile and the ground truth. The IoUs of semicircle and pentagon are the highest at 90%, while the lowest IoU of the complicated inverted-T-shape is still at 83%.

We also implement a simple shape classifier and use its accuracy as an alternative measure of the target profiling accuracy. Compared to MAE and IoU, this measure is more relevant to downstream applications such as target identification. Specifically, we calculate the MAE between the

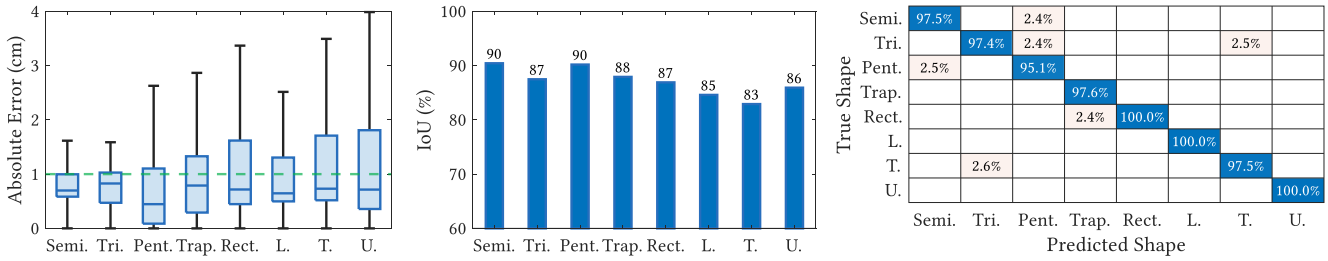

(a) Box plot of absolute error. **(b) IoU.** **(c) Confusion matrix.**

Figure 14: Overall Performance.

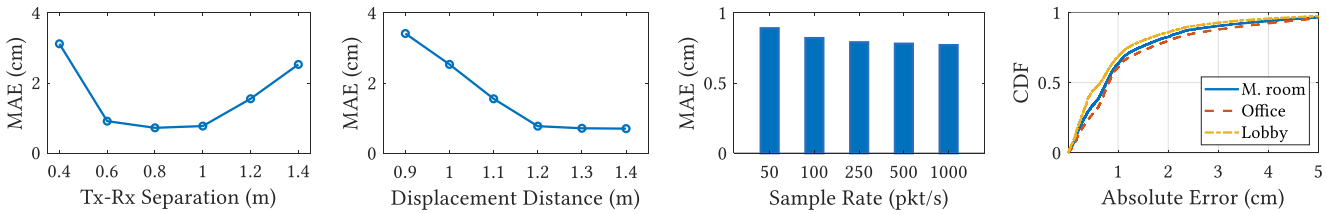

(a) Tx-Rx Separation. **(b) Displacement distance.** **(c) Sample rate.** **(d) CDF of three environments.**

Figure 15: Impacts of experimental conditions.

estimated profile and all eight ground truth shapes, and output the shape with the lowest MAE as the prediction. Figure 14c shows the classification accuracy. For each shape, the accuracy is larger than 95%. The classification accuracy of rectangle, L-shape and U-shape are 100% because they are quite different from the others. On the other hand, semicircle and pentagon can sometimes be confused with one another, and trapezoid is occasionally classified as rectangle. This can again be attributed to the windowing effect that hinders the precise estimation of sharp side edges, resulting in potential confusion amongst these similar shapes.

4.3 Impacts of Experimental Conditions

Next, we investigate the impacts of experimental conditions on WiProfile's performance of target profiling, including the Tx-Rx separation, displacement distance, sample rate, and surrounding environment.

4.3.1 Impacts of Tx-Rx Separation. In this set of experiments, we increase the Tx-Rx separation from 0.4 m to 1.4 m, with a step size of 0.2 m. Figure 15a shows that the MAEs of WiProfile first decrease but then increase. A longer Tx-Rx separation contributes to a larger maximum height, but lower profiling accuracy, as discussed in Section 2.3. For the smallest Tx-Rx separation at 0.4 m, the maximum height allowable is 12.7 cm, lower than the target height. As a result, the MAE is large as well. Thus, to achieve a higher level of profiling accuracy, an appropriate Tx-Rx separation should be chosen based on the rough dimension of the target.

4.3.2 Impacts of Displacement Distance. In this set of experiments, we increase the displacement distance from 0.9 m to 1.4 m, with a step size of 0.1 m. Figure 15b shows that the MAEs of WiProfile decrease when the displacement distance increases from 0.9 m to 1.2 m, and almost level off when it is above 1.2 m. This is consistent with the analysis in Section 2.3. Namely, 1) a larger displacement distance increases accuracy; and 2) as the target moves farther from the LoS path, the amount of diffraction rapidly diminishes. However, thanks to the tiny reflection areas of the thin metal plates, the reflected signals remain relatively low and thus do not have a much adverse effect on profile estimations, even when the target is 0.7 m (a half of 1.4 m) away from the LoS path.

4.3.3 Impacts of Sample Rate. In this set of experiments, we vary the packet transmission rate of the WiFi transmitter to increase the sample rate of CSI readings from 50 Hz to 1000 Hz, while the target speed remains the same at 0.12 m/s. Figure 15c shows that WiProfile can achieve accurate target profiling over a wide range of sample rates. For example, halving the sample rate from 100 Hz to 50 Hz only results in an increase of 0.1 cm in MAE. Note that the sample rate (samples per second) should be chosen in accordance with the target speed (displacement distance per second). As a general rule of thumb, a total of 142 samples per meter can yield good accuracy. When the target moves faster, the minimal sample rate needs to be scaled up accordingly.

4.3.4 Impacts of Surrounding Environment. In this set of experiments, we test WiProfile in the three different indoor

environments illustrated in Figure 12. Figure 15d shows Cumulative Distribution Function (CDF) of the absolute errors for all shapes in three environments. As can be seen, WiProfile performs robustly and consistently across different environments. The performance in the lobby environment is slightly better because the environment is more open and has less multipath reflections.

4.4 Experiments on Everyday Objects

To assess the versatility of WiProfile in practice, we further evaluate it using everyday objects of diverse shapes, sizes, and materials, as listed in Table 3.

Table 3: Test objects.

Object	Shape	Width	Height	Material
A steel bowl	Trapezoid	24 cm	10 cm	Metal
A zip-top can	Rectangle	6 cm	12 cm	Metal
A piece of rock	Trapezoid	20 cm	10 cm	Granite
A wireless mouse	Triangle	12 cm	5 cm	Rubber, plastic
A bottle of drink	Pentagon	9 cm	17 cm	Water, plastic
Two bottles of water	Rectangle	12 cm	16 cm	Water, plastic
A coconut	Rectangle	11 cm	11 cm	Water, wood
A bunch of grapes	Triangle	18 cm	10 cm	Water, wood

4.4.1 Metal Objects. Figure 16 depicts the estimated profiles for a steel bowl and a metal zip-top can. The estimation for the steel bowl agrees well with the actual profile in part due to its slanted sides. A larger deviation is observed in the sides of the zip-top can, which can be attributed to its narrow width and long vertical sides. However, the MAE of 0.77 cm remains below 1 cm, indicating a high profiling accuracy.

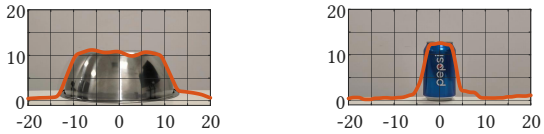

(a) A steel bowl. **(b) A zip-top can.**

Figure 16: Estimated profiles of metal objects.

4.4.2 Non-metallic Objects. Figure 17 shows the estimated profiles for a piece of rock and a wireless mouse with a rubber and plastic shell. The estimated profiles agree very well with the actual profiles in both cases.

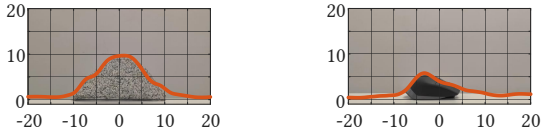

(a) A piece of rock. **(b) A wireless mouse.**

Figure 17: Estimated profiles of non-metallic objects.

4.4.3 Liquids. Figure 18 shows the estimated profiles for a bottle of soft drink and two bottles of water side-by-side. Again, the estimated profiles generally agree well with the actual profiles of the liquids except for the rolling edges. Note that the target shapes here are corresponding to actually the contours of liquid inside the containers. The top of the bottles, above the liquid level, is made of plastic with relatively weak diffraction and is undetected.

(a) A bottle of soft drink. **(b) Two bottles of water.**

Figure 18: Estimated profiles of liquids.

4.4.4 Fruits. We further test WiProfile on a coconut and a bunch of grapes, both composed mostly of water. The estimated profiles are shown in Figure 19. Despite the uneven surfaces of both objects, the results are quite encouraging. We conclude that WiProfile can indeed work well over a variety of objects of diverse shapes, sizes, and materials.

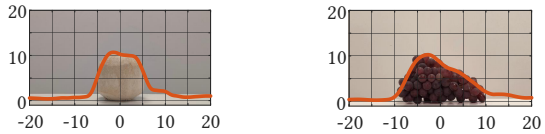

(a) A coconut. **(b) A bunch of grapes.**

Figure 19: Estimated profiles of fruits.

5 DISCUSSION

In this section, we discuss the limitations and possible extensions to WiProfile.

Restrictions on the target: To be accurately profiled by WiProfile, restrictions on the target material, size and profile shape should be in place:

- Material: The target should fully block the RF signal transmission. In other words, the target material is either metal or non-metal with large permittivity at the WiFi frequency band (e.g., water). In instances where a significant portion of the signal penetrates the target, the received signal contains both diffraction and direct transmission. Thus, it is influenced not only by the profile but also by the permittivity and the thickness of the target [7, 38, 43], in which case a different signal model should be adopted.
- Size: The target size should fall in a proper range. Specifically, the smallest discriminable diameter is half-wavelength (3 cm for 5 GHz WiFi), the maximum height is given by Equation (19), and the maximum width corresponds to half the length of the Tx-Rx separation.

• Profile Shape: The target profile should be flat-bottomed and be free of internal holes as WiProfile estimates the differences between the upper and bottom contours. For more general shapes, the estimated profile may deviate from the actual target profile.

Removal of the feeder line: The feeder line, as part of the novel antenna placement strategy, allows the connected reference Rx antenna to be co-located with the Tx antenna. The arrangement provides a reference CSI to combat synchronization errors. While enabling target profiling on commodity devices, the use of a feed line introduces extra cost and additional system requirements, potentially limiting the real world applications of the proposed system. Exploring approaches to remove the feeder line will be an important venue for future research. For example, MultiSense [48], which constructs a reference CSI by combing CSIs from multiple antennas pairs, presents a promising direction.

Beyond controlled linear target motion: To achieve optimal performance, WiProfile employs a controlled setup, where a target moves at a constant velocity along a linear trajectory between the transceivers. However, as long as the positions of the target are known at the time of packet receptions and the packet transmission rate is sufficiently high, variations in target speeds can be accommodated. Such conditions can be satisfied in industrial settings such as conveyor belt systems. Investigating the impacts of positioning errors on target profiling and extending WiProfile to non-linear motions will be important venues for future research.

Applicability to other RF technologies: In this paper, WiProfile is implemented and evaluated using commodity WiFi devices in the 5 GHz band. Actually, the proposed CSI-Profile model and WiProfile are applicable to other frequency bands of common wireless systems (e.g., 4G, 5G, UWB, and LoRa), from several hundred MHz to several GHz. Generally speaking, employing higher frequency radios and smaller Tx-Rx separation imply smaller target sizes but more accurate estimation. The opposite is true for RF technologies at lower frequency ranges such as LoRa.

6 RELATED WORK

In recent years, there are several research works on imaging objects with RF signals. Based on the type of devices employed, these approaches can be grouped into two major categories: radar-based target imaging and WiFi-based target imaging.

Radar-based target imaging: The basic idea behind radar-based target imaging is to reconstruct a target's point cloud by precisely measuring parameters of reflected signals, such as Time of Flight (ToF), Angle of Arrival (AoA), and Doppler Frequency Shift (DFS). Prior research endeavors [1, 32, 41, 47, 54, 55] have commonly utilized ultra-wideband (UWB) or mmWave monostatic radars equipped with multiple antennas to achieve finer spatial resolution. For instance, RF-Capture [1] employs a 1.78 GHz bandwidth and an antenna array of 4×16 to capture basic skeletal information of a human target concealed behind a wall. MilliPoint [32], on the other hand, leverages a commercial mmWave radar featuring 4 GHz bandwidth and an antenna array of 6×8, achieving a median error below 5 cm for height estimation.

While UWB or mmWave radars can achieve high ranging accuracy due to their expansive operational bandwidth, their spatial resolution remains constrained by the number of antennas. To further increase spatial resolution, movements of the radar or the target can be exploited. The relative movements between the two create a large virtual array and thus allow "synthesizing" higher resolution images [32, 41, 47].

WiProfile bares some similarity with Inverse Synthetic Aperture Radar (ISAR) imaging in utilizing target movements. However, it works on a different principle – diffraction as opposed to reflection. Furthermore, the significantly narrower operational bandwidth and spatially separated Tx and Rx devices make imaging using WiFi devices much more challenging.

WiFi-based target imaging: Prior efforts in WiFi-based target imaging predominantly center on utilizing signal reflection [12, 14, 16, 31, 34] and penetration [6, 15]. With reflected signals, to mitigate the limited spatial resolution due to the low frequency (e.g., 5 GHz), narrow bandwidth (e.g., 20 MHz), and the limited number of antennas (e.g., three) of commodity WiFi devices, some works move Rx antennas to create virtual antenna arrays [12, 31]. Though showing promising results in detecting and localizing objects, existing approaches fall short of capturing finer details, such as object shape or size.

Another line of approaches leverage the inherent ability of WiFi signals to penetrate non-metallic objects and generate images of the cross-sections of objects [6, 15]. By placing a pair of Tx and Rx on the opposite sides of a target and moving them together, one records the amounts of amplitude and phase changes as the signal penetrates the target. The cross-sectional image of the target is then estimated using tomographic scanning techniques. However, several limitations in such methods restrict their adoption in real-world applications. First, the movements of the Tx and Rx have to be tightly coordinated and synchronized, adding to hardware costs. Second, these methods only work with uniform objects of known material. Lastly, they fail in case of non-penetrable objects such as those encased in metallic shells.

In contrast, WiProfile can work with objects of a variety of materials including non-uniform ones. Furthermore, WiProfile leverages movements of the target instead of the transceivers, which has relatively low deployment costs in certain scenarios.

7 CONCLUSION

In this paper, we presented the first work that harnesses the diffraction effects of WiFi signals for fine-grained target profiling. We introduced a CSI-Profile model to characterize the relationship between the CSI measured at different target positions and the target profile, and showed a robust solution to determine the target profile by the inverse Fresnel transform. Additionally, we proposed a novel antenna placement strategy to mitigate CSI measurement errors on commodity WiFi devices. Comprehensive experiments demonstrated that the proposed WiProfile system could accurately reconstruct profiles with MAEs of less than 1 cm under various conditions, and effectively estimate the profiles of everyday objects of diverse shapes, sizes, and materials. Overall, our work opens up new directions for fine-grained target imaging using RF signals.

ACKNOWLEDGMENTS

We would like to sincerely thank the reviewers and shepherd for their valuable feedback. This research is supported by the NSFC A3 Foresight Program (No. 62061146001), the PKU-NTU Collaboration Project, and the European Union through the Horizon EIC pathfinder challenge project SUSTAIN (No. 101071179).

A DETAILED DERIVATIONS

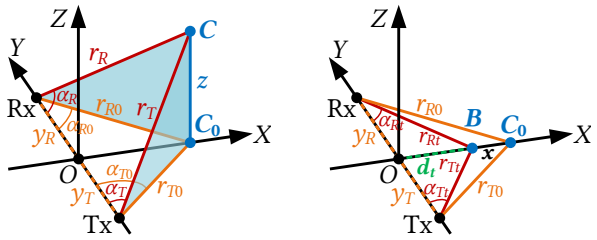

(a) Equation (6). **(b) Equation (15).**

Figure 20: Geometrical relations.

A.1 Derivation of Equation (6)

As illustrated in Figure 20a, the projection of any point C with coordinates of $(x + d_t, 0, z)$ on the X-Y plane is at point C_0 with coordinates of $(x + d_t, 0, 0)$. Accordingly, $r_{T0} = r_T(x + d_t, 0)$, $r_{R0} = r_R(x + d_t, 0)$, $\alpha_{T0} = \alpha_T(x + d_t, 0)$, $\alpha_{R0} = \alpha_R(x + d_t, 0)$. When $z \ll y_T$, using the Taylor series expansion, we have the following approximation: $r_T(x + d_t, z) = \sqrt{r_{T0}^2 + z^2} = r_{T0}\sqrt{1 + \frac{z^2}{r_{T0}^2}} \approx r_{T0} + \frac{z^2}{2r_{T0}} \approx r_{T0} + \frac{z^2}{2y_T}$. Similarly, when $z \ll y_R$, $r_R(x + d_t, z) \approx r_{R0} + \frac{z^2}{2y_R}$.

Omitting high order terms and letting $\rho_0 = \frac{1}{2y_T} + \frac{1}{2y_R}$, we have:

- $r_T(x + d_t, z)\, r_R(x + d_t, z) \approx r_{T0}\, r_{R0}$,
- $r_T(x + d_t, z) + r_R(x + d_t, z) \approx r_{T0} + r_{R0} + \rho_0 z^2$,
- $\cos\alpha_T(x + d_t, z) + \cos\alpha_R(x + d_t, z) \approx \cos\alpha_{T0} + \cos\alpha_{R0}$.

Substituting the approximations into Equation (3), it gives

$$
\begin{aligned}
f(x + d_t, z) &\approx \frac{A}{2j\lambda}\frac{\cos\alpha_{T0} + \cos\alpha_{R0}}{r_{T0}\, r_{R0}} e^{-jk(r_{T0} + r_{R0} + \rho_0 z^2)} \\
&= \frac{A}{2j\lambda}\frac{\cos\alpha_{T0} + \cos\alpha_{R0}}{r_{T0}\, r_{R0}} e^{-jk(r_{T0} + r_{R0})} e^{-jk\rho_0 z^2} \\
&= f(x + d_t, 0) e^{-jk\rho_0 z^2}.
\end{aligned}
$$

A.2 Derivation of Equation (15)

As illustrated in Figure 20b, point B is at $(d_t, 0, 0)$, and point C_0 is at $(x + d_t, 0, 0)$. When $x \ll y_T$, using the Taylor series expansion, we have the following approximation: $r_{T0} = \sqrt{y_T^2 + (x + d_t)^2} = \sqrt{(y_T^2 + d_t^2) + x^2 + 2d_t x} = \sqrt{r_{Tt}^2 + x^2 + 2d_t x}$ $= r_{Tt}\sqrt{1 + \frac{x^2 + 2d_t x}{r_{Tt}^2}} \approx r_{Tt} + \frac{x^2 + 2d_t x}{2r_{Tt}} \approx r_{Tt} + \frac{x^2 + 2d_t x}{2y_T}$. Similarly, when $x \ll y_R$, $r_{R0} \approx r_{Rt} + \frac{x^2 + 2d_t x}{2y_R}$.

Omitting high order terms, we have:

- $r_{T0}\, r_{R0} \approx r_{Tt}\, r_{Rt}$,
- $r_{T0} + r_{R0} \approx r_{Tt} + r_{Rt} + \rho_0\left(x^2 + 2d_t x\right)$,
- $\cos\alpha_{T0} + \cos\alpha_{R0} \approx \cos\alpha_{Tt} + \cos\alpha_{Rt}$.

Substituting the approximations into Equation (12), it gives

$$
\begin{aligned}
D(x + d_t) &= \frac{A}{2j\lambda}\frac{\cos\alpha_{T0} + \cos\alpha_{R0}}{r_{T0}\, r_{R0}} e^{-jk(r_{T0} + r_{R0})} \\
&\approx \frac{A}{2j\lambda}\frac{\cos\alpha_{Tt} + \cos\alpha_{Rt}}{r_{Tt}\, r_{Rt}} e^{-jk\left[r_{Tt} + r_{Rt} + \rho_0\left(x^2 + 2d_t x\right)\right]} \\
&= \frac{A}{2j\lambda}\frac{\cos\alpha_{Tt} + \cos\alpha_{Rt}}{r_{Tt}\, r_{Rt}} e^{-jk(r_{Tt} + r_{Rt})} e^{-jk\rho_0\left(x^2 + 2d_t x\right)} \\
&= D(d_t) e^{-jk\rho_0\left(x^2 + 2d_t x\right)}.
\end{aligned}
$$

REFERENCES

[1] Fadel Adib, Chen-Yu Hsu, Hongzi Mao, Dina Katabi, and Frédo Durand. 2015. Capturing the Human Figure through a Wall. *ACM Trans. Graph.* 34, 6, Article 219 (Nov. 2015), 13 pages. https://doi.org/10.1145/2816795.2818072

[2] Max Born and Emil Wolf. 2019. *Principles of Optics.* Cambridge University Press, New York, NY, USA.

[3] V.V. Chapurskiy and V.N. Sablin. 2000. SISAR: Shadow Inverse Synthetic Aperture Radiolocation. In *Record of the IEEE 2000 International Radar Conference [Cat. No. 00CH37037].* IEEE, New York, NY, USA, 322–328. https://doi.org/10.1109/RADAR.2000.851854

[4] Fabiola Colone, Debora Pastina, Paolo Falcone, and Pierfrancesco Lombardo. 2014. WiFi-Based Passive ISAR for High-Resolution Cross-Range Profiling of Moving Targets. *IEEE Transactions on Geoscience and Remote Sensing* 52, 6 (2014), 3486–3501. https://doi.org/10.1109/TGRS.2013.2273099

[5] Mango Communications. 2012. WARP Project. https://warpproject.org

[6] Saandeep Depatla, Lucas Buckland, and Yasamin Mostofi. 2015. X-Ray Vision With Only WiFi Power Measurements Using Rytov Wave Models. *IEEE Transactions on Vehicular Technology* 64, 4 (2015), 1376–1387. https://doi.org/10.1109/TVT.2015.2397446

[7] Ashutosh Dhekne, Mahanth Gowda, Yixuan Zhao, Haitham Hassanieh, and Romit Roy Choudhury. 2018. LiquID: A Wireless Liquid IDentifier. In *Proceedings of the 16th Annual International Conference on Mobile Systems, Applications, and Services* (Munich, Germany) *(MobiSys '18)*. ACM, New York, NY, USA, 442–454. https://doi.org/10.1145/3210240.3210345

[8] Ruiyang Gao, Wenwei Li, Yaxiong Xie, Enze Yi, Leye Wang, Dan Wu, and Daqing Zhang. 2022. Towards Robust Gesture Recognition by Characterizing the Sensing Quality of WiFi Signals. *Proc. ACM Interact. Mob. Wearable Ubiquitous Technol.* 6, 1, Article 11 (March 2022), 26 pages. https://doi.org/10.1145/3517241

[9] Ruiyang Gao, Mi Zhang, Jie Zhang, Yang Li, Enze Yi, Dan Wu, Leye Wang, and Daqing Zhang. 2021. Towards Position-Independent Sensing for Gesture Recognition with Wi-Fi. *Proc. ACM Interact. Mob. Wearable Ubiquitous Technol.* 5, 2, Article 61 (June 2021), 28 pages. https://doi.org/10.1145/3463504

[10] D. Halperin, W. Hu, A. Sheth, and D. Wetherall. 2011. Tool Release: Gathering 802.11N Traces with Channel State Information. *SIGCOMM Comput. Commun. Rev.* 41, 1 (Jan. 2011), 53–53. https://doi.org/10.1145/1925861.1925870

[11] Hristo D. Hristov. 2000. *Fresnal Zones in Wireless Links, Zone Plate Lenses and Antennas.* Artech House, Inc., Norwood, MA, USA.

[12] Donny Huang, Rajalakshmi Nandakumar, and Shyamnath Gollakota. 2014. Feasibility and Limits of Wi-Fi Imaging. In *Proceedings of the 12th ACM Conference on Embedded Network Sensor Systems* (Memphis, Tennessee) *(SenSys '14)*. ACM, New York, NY, USA, 266–279. https://doi.org/10.1145/2668332.2668344

[13] Satoshi Ito and Yoshifumi Yamada. 2008. Alias-free image reconstruction using Fresnel transform in the phase-scrambling Fourier imaging technique. *Magnetic Resonance in Medicine* 60, 2 (2008), 422–430. https://doi.org/10.1002/mrm.21672

[14] Wenjun Jiang, Hongfei Xue, Chenglin Miao, Shiyang Wang, Sen Lin, Chong Tian, Srinivasan Murali, Haochen Hu, Zhi Sun, and Lu Su. 2020. Towards 3D Human Pose Construction Using WiFi. In *Proceedings of the 26th Annual International Conference on Mobile Computing and Networking* (London, United Kingdom) *(MobiCom '20)*. ACM, New York, NY, USA, Article 23, 14 pages. https://doi.org/10.1145/3372224.3380900

[15] Chitra R. Karanam and Yasamin Mostofi. 2017. 3D Through-Wall Imaging with Unmanned Aerial Vehicles Using WiFi. In *Proceedings of The 16th ACM/IEEE International Conference on Information Processing in Sensor Networks* (Pittsburgh, Pennsylvania) *(IPSN '17)*. ACM, New York, NY, USA, 131–142. https://doi.org/10.1145/3055031.3055084

[16] Chenning Li, Zheng Liu, Yuguang Yao, Zhichao Cao, Mi Zhang, and Yunhao Liu. 2020. Wi-Fi See It All: Generative Adversarial Network-Augmented Versatile Wi-Fi Imaging. In *Proceedings of the 18th Conference on Embedded Networked Sensor Systems* (Virtual Event, Japan) *(SenSys '20)*. ACM, New York, NY, USA, 436–448. https://doi.org/10.1145/3384419.3430725

[17] Shengjie Li, Xiang Li, Qin Lv, Guiyu Tian, and Daqing Zhang. 2018. WiFit: Ubiquitous Bodyweight Exercise Monitoring with Commodity Wi-Fi Devices. In *2018 IEEE SmartWorld, Ubiquitous Intelligence & Computing, Advanced & Trusted Computing, Scalable Computing & Communications, Cloud & Big Data Computing, Internet of People and Smart City Innovation (SmartWorld/SCALCOM/UIC/ATC/CBDCom/IOP/SCI)*. IEEE, New York, NY, USA, 530–537. https://doi.org/10.1109/SmartWorld.2018.00114

[18] Shengjie Li, Xiang Li, Kai Niu, Hao Wang, Yue Zhang, and Daqing Zhang. 2017. AR-Alarm: An Adaptive and Robust Intrusion Detection System Leveraging CSI from Commodity Wi-Fi. In *Enhanced Quality of Life and Smart Living*, Mounir Mokhtari, Bessam Abdulrazak, and Hamdi Aloulou (Eds.). Springer International Publishing, Cham, 211–223.

[19] Shengjie Li, Zhaopeng Liu, Yue Zhang, Qin Lv, Xiaopeng Niu, Leye Wang, and Daqing Zhang. 2020. WiBorder: Precise Wi-Fi Based Boundary Sensing via Through-Wall Discrimination. *Proc. ACM Interact. Mob. Wearable Ubiquitous Technol.* 4, 3, Article 89 (Sept. 2020), 30 pages. https://doi.org/10.1145/3411834

[20] Xiang Li, Shengjie Li, Daqing Zhang, Jie Xiong, Yasha Wang, and Hong Mei. 2016. Dynamic-MUSIC: Accurate Device-Free Indoor Localization. In *Proceedings of the 2016 ACM International Joint Conference on Pervasive and Ubiquitous Computing* (Heidelberg, Germany) *(UbiComp '16)*. ACM, New York, NY, USA, 196–207. https://doi.org/10.1145/2971648.2971665

[21] Xiang Li, Daqing Zhang, Qin Lv, Jie Xiong, Shengjie Li, Yue Zhang, and Hong Mei. 2017. IndoTrack: Device-Free Indoor Human Tracking with Commodity Wi-Fi. *Proc. ACM Interact. Mob. Wearable Ubiquitous Technol.* 1, 3, Article 72 (Sept. 2017), 22 pages. https://doi.org/10.1145/3130940

[22] Yang Li, Dan Wu, Jie Zhang, Xuhai Xu, Yaxiong Xie, Tao Gu, and Daqing Zhang. 2022. DiverSense: Maximizing Wi-Fi Sensing Range Leveraging Signal Diversity. *Proc. ACM Interact. Mob. Wearable Ubiquitous Technol.* 6, 2, Article 94 (July 2022), 28 pages. https://doi.org/10.1145/3536393

[23] Jinyi Liu, Youwei Zeng, Tao Gu, Leye Wang, and Daqing Zhang. 2021. WiPhone: Smartphone-Based Respiration Monitoring Using Ambient Reflected WiFi Signals. *Proc. ACM Interact. Mob. Wearable Ubiquitous Technol.* 5, 1, Article 23 (March 2021), 19 pages. https://doi.org/10.1145/3448092

[24] Kai Niu, Xuanzhi Wang, Fusang Zhang, Rong Zheng, Zhiyun Yao, and Daqing Zhang. 2022. Rethinking Doppler Effect for Accurate Velocity Estimation With Commodity WiFi Devices. *IEEE Journal on Selected Areas in Communications* 40, 7 (2022), 2164–2178. https://doi.org/10.1109/JSAC.2022.3155523

[25] Kai Niu, Fusang Zhang, Yuhang Jiang, Jie Xiong, Qin Lv, Youwei Zeng, and Daqing Zhang. 2019. WiMorse: A Contactless Morse Code Text Input System Using Ambient WiFi Signals. *IEEE Internet of Things Journal* 6, 6 (Dec. 2019), 9993–10008. https://doi.org/10.1109/JIOT.2019.2934904

[26] Kai Niu, Fusang Zhang, Jie Xiong, Xiang Li, Enze Yi, and Daqing Zhang. 2018. Boosting Fine-Grained Activity Sensing by Embracing Wireless Multipath Effects. In *Proceedings of the 14th International Conference on Emerging Networking EXperiments and Technologies* (Heraklion, Greece) *(CoNEXT '18)*. ACM, New York, NY, USA, 139–151. https://doi.org/10.1145/3281411.3281425

[27] Thomas O'Haver. 2023. *A Pragmatic Introduction to Signal Processing*. University of Maryland, College Park, MD, USA.

[28] Alan V. Oppenheim and Ronald W. Schafer. 2009. *Discrete-Time Signal Processing*. Prentice Hall Press, Upper Saddle River, NJ, USA.

[29] Caner Özdemir. 2021. *Inverse Synthetic Aperture Radar Imaging with MATLAB Algorithms*. John Wiley & Sons, Inc., Hoboken, NJ, USA.

[30] Sameera Palipana, David Rojas, Piyush Agrawal, and Dirk Pesch. 2018. FallDeFi: Ubiquitous Fall Detection Using Commodity Wi-Fi Devices. *Proc. ACM Interact. Mob. Wearable Ubiquitous Technol.* 1, 4, Article 155 (Dec. 2018), 25 pages. https://doi.org/10.1145/3161183

[31] Anurag Pallaprolu, Belal Korany, and Yasamin Mostofi. 2022. Wiffract: A New Foundation for RF Imaging via Edge Tracing. In *Proceedings of the 28th Annual International Conference on Mobile Computing And Networking* (Sydney, NSW, Australia) *(MobiCom '22)*. ACM, New York, NY, USA, 255–267. https://doi.org/10.1145/3495243.3514261

[32] Kun Qian, Zhaoyuan He, and Xinyu Zhang. 2020. 3D Point Cloud Generation with Millimeter-Wave Radar. *Proc. ACM Interact. Mob. Wearable Ubiquitous Technol.* 4, 4, Article 148 (Dec. 2020), 23 pages. https://doi.org/10.1145/3432221

[33] Kun Qian, Chenshu Wu, Yi Zhang, Guidong Zhang, Zheng Yang, and Yunhao Liu. 2018. Widar2.0: Passive Human Tracking with a Single Wi-Fi Link. In *Proceedings of the 16th Annual International Conference on Mobile Systems, Applications, and Services* (Munich, Germany) *(MobiSys '18)*. ACM, New York, NY, USA, 350–361. https://doi.org/10.1145/3210240.3210314

[34] Yili Ren, Zi Wang, Yichao Wang, Sheng Tan, Yingying Chen, and Jie Yang. 2022. GoPose: 3D Human Pose Estimation Using WiFi. *Proc. ACM Interact. Mob. Wearable Ubiquitous Technol.* 6, 2, Article 69 (July 2022), 25 pages. https://doi.org/10.1145/3534605

[35] Mark A. Richards, James A. Scheer, and William A. Holm. 2010. *Principles of Modern Radar*. Vol. 1. SciTech Publishing, Raleigh, NC, USA.

[36] Hao Wang, Daqing Zhang, Junyi Ma, Yasha Wang, Yuxiang Wang, Dan Wu, Tao Gu, and Bing Xie. 2016. Human Respiration Detection with Commodity WiFi Devices: Do User Location and Body Orientation Matter?. In *Proceedings of the 2016 ACM International Joint Conference on Pervasive and Ubiquitous Computing* (Heidelberg, Germany) *(UbiComp '16)*. ACM, New York, NY, USA, 25–36. https://doi.org/10.1145/2971648.2971744

[37] Hao Wang, Daqing Zhang, Yasha Wang, Junyi Ma, Yuxiang Wang, and Shengjie Li. 2017. RT-Fall: A Real-Time and Contactless Fall Detection System with Commodity WiFi Devices. *IEEE Transactions on Mobile Computing* 16, 2 (2017), 511–526. https://doi.org/10.1109/TMC.2016.2557795

[38] Ju Wang, Jie Xiong, Xiaojiang Chen, Hongbo Jiang, Rajesh Krishna Balan, and Dingyi Fang. 2017. TagScan: Simultaneous Target Imaging and Material Identification with Commodity RFID Devices. In *Proceedings of the 23rd Annual International Conference on Mobile Computing and Networking* (Snowbird, Utah, USA) *(MobiCom '17)*. ACM, New York, NY, USA, 288–300. https://doi.org/10.1145/3117811.3117830

[39] Xuanzhi Wang, Kai Niu, Jie Xiong, Bochong Qian, Zhiyun Yao, Tairong Lou, and Daqing Zhang. 2022. Placement Matters: Understanding the Effects of Device Placement for WiFi Sensing. *Proc. ACM Interact. Mob. Wearable Ubiquitous Technol.* 6, 1, Article 32 (March 2022), 25 pages. https://doi.org/10.1145/3517237

[40] Xuanzhi Wang, Kai Niu, Anlan Yu, Jie Xiong, Zhiyun Yao, Junzhe Wang, Wenwei Li, and Daqing Zhang. 2023. WiMeasure: Millimeter-Level Object Size Measurement with Commodity WiFi Devices. *Proc. ACM Interact. Mob. Wearable Ubiquitous Technol.* 7, 2, Article 79 (June 2023), 26 pages. https://doi.org/10.1145/3596250

[41] Claire M. Watts, Patrick Lancaster, Andreas Pedross-Engel, Joshua R. Smith, and Matthew S. Reynolds. 2016. 2D and 3D millimeter-wave synthetic aperture radar imaging on a PR2 platform. In *2016 IEEE/RSJ International Conference on Intelligent Robots and Systems (IROS)*. IEEE, New York, NY, USA, 4304–4310. https://doi.org/10.1109/IROS.2016.7759633

[42] Dan Wu, Ruiyang Gao, Youwei Zeng, Jinyi Liu, Leye Wang, Tao Gu, and Daqing Zhang. 2020. FingerDraw: Sub-Wavelength Level Finger Motion Tracking with WiFi Signals. *Proc. ACM Interact. Mob. Wearable Ubiquitous Technol.* 4, 1, Article 31 (March 2020), 27 pages. https://doi.org/10.1145/3380981

[43] Binbin Xie, Jie Xiong, Xiaojiang Chen, Eugene Chai, Liyao Li, Zhanyong Tang, and Dingyi Fang. 2019. Tagtag: Material Sensing with Commodity RFID. In *Proceedings of the 17th Conference on Embedded Networked Sensor Systems* (New York, New York) *(SenSys '19)*. ACM, New York, NY, USA, 338–350. https://doi.org/10.1145/3356250.3360027

[44] Yaxiong Xie, Zhenjiang Li, and Mo Li. 2015. Precise Power Delay Profiling with Commodity WiFi. In *Proceedings of the 21st Annual International Conference on Mobile Computing and Networking* (Paris, France) *(MobiCom '15)*. ACM, New York, NY, USA, 53–64. https://doi.org/10.1145/2789168.2790124

[45] Yaxiong Xie, Jie Xiong, Mo Li, and Kyle Jamieson. 2019. MD-Track: Leveraging Multi-Dimensionality for Passive Indoor Wi-Fi Tracking. In *The 25th Annual International Conference on Mobile Computing and Networking* (Los Cabos, Mexico) *(MobiCom '19)*. ACM, New York, NY, USA, Article 8, 16 pages. https://doi.org/10.1145/3300061.3300133

[46] Tong Xin, Bin Guo, Zhu Wang, Pei Wang, Jacqueline Chi Kei Lam, Victor Li, and Zhiwen Yu. 2018. FreeSense: A Robust Approach for Indoor Human Detection Using Wi-Fi Signals. *Proc. ACM Interact. Mob. Wearable Ubiquitous Technol.* 2, 3, Article 143 (Sept. 2018), 23 pages. https://doi.org/10.1145/3264953

[47] Muhammet Emin Yanik and Murat Torlak. 2019. Near-Field 2-D SAR Imaging by Millimeter-Wave Radar for Concealed Item Detection. In *2019 IEEE Radio and Wireless Symposium (RWS)*. IEEE, New York, NY, USA, 1–4. https://doi.org/10.1109/RWS.2019.8714552

[48] Youwei Zeng, Dan Wu, Jie Xiong, Jinyi Liu, Zhaopeng Liu, and Daqing Zhang. 2020. MultiSense: Enabling Multi-Person Respiration Sensing with Commodity WiFi. *Proc. ACM Interact. Mob. Wearable Ubiquitous Technol.* 4, 3, Article 102 (Sept. 2020), 29 pages. https://doi.org/10.1145/3411816

[49] Youwei Zeng, Dan Wu, Jie Xiong, Enze Yi, Ruiyang Gao, and Daqing Zhang. 2019. FarSense: Pushing the Range Limit of WiFi-Based Respiration Sensing with CSI Ratio of Two Antennas. *Proc. ACM Interact. Mob. Wearable Ubiquitous Technol.* 3, 3, Article 121 (Sept. 2019), 26 pages. https://doi.org/10.1145/3351279

[50] Youwei Zeng, Dan Wu, Jie Xiong, and Daqing Zhang. 2021. Boosting WiFi Sensing Performance via CSI Ratio. *IEEE Pervasive Computing* 20, 1 (Jan. 2021), 62–70. https://doi.org/10.1109/MPRV.2020.3041024

[51] Fusang Zhang, Kai Niu, Jie Xiong, Beihong Jin, Tao Gu, Yuhang Jiang, and Daqing Zhang. 2019. Towards a Diffraction-Based Sensing Approach on Human Activity Recognition. *Proc. ACM Interact. Mob. Wearable Ubiquitous Technol.* 3, 1, Article 33 (March 2019), 25 pages. https://doi.org/10.1145/3314420

[52] Feng Zhang, Chenshu Wu, Beibei Wang, Hung-Quoc Lai, Yi Han, and K. J. Ray Liu. 2019. WiDetect: Robust Motion Detection with a Statistical Electromagnetic Model. *Proc. ACM Interact. Mob. Wearable Ubiquitous Technol.* 3, 3, Article 122 (Sept. 2019), 24 pages. https://doi.org/10.1145/3351280

[53] Fusang Zhang, Daqing Zhang, Jie Xiong, Hao Wang, Kai Niu, Beihong Jin, and Yuxiang Wang. 2018. From Fresnel Diffraction Model to Fine-Grained Human Respiration Sensing with Commodity Wi-Fi Devices. *Proc. ACM Interact. Mob. Wearable Ubiquitous Technol.* 2, 1, Article 53 (March 2018), 23 pages. https://doi.org/10.1145/3191785

[54] Mingmin Zhao, Tianhong Li, Mohammad Abu Alsheikh, Yonglong Tian, Hang Zhao, Antonio Torralba, and Dina Katabi. 2018. Through-Wall Human Pose Estimation Using Radio Signals. In *2018 IEEE/CVF Conference on Computer Vision and Pattern Recognition*. IEEE, New York, NY, USA, 7356–7365. https://doi.org/10.1109/CVPR.2018.00768

[55] Mingmin Zhao, Yonglong Tian, Hang Zhao, Mohammad Abu Alsheikh, Tianhong Li, Rumen Hristov, Zachary Kabelac, Dina Katabi, and Antonio Torralba. 2018. RF-Based 3D Skeletons. In *Proceedings of the 2018 Conference of the ACM Special Interest Group on Data Communication* (Budapest, Hungary) *(SIGCOMM '18)*. ACM, New York, NY, USA, 267–281. https://doi.org/10.1145/3230543.3230579